Time resolving the photoelectron motion driven by the magnetic component of a laser field

Jintai Liang ⊙,[1] Weiliang Wang,[1] Kunlong Liu ⊙,[1] Wei-Chao Jiang,[2] Lianbo Guo,[1,*] Yueming Zhou ⊙,[1,†] and Peixiang Lu[1,3]

[1]*Wuhan National Laboratory for Optoelectronics and School of Physics, Huazhong University of Science and Technology,*
Wuhan 430074, China

[2]*Institute of Quantum Precision Measurement, College of Physics and Optoelectronic Engineering, Shenzhen University,*
Shenzhen 518060, China

[3]*Optics Valley Laboratory, Hubei 430074, China*

In photoionization, the nondipole interactions induce forward-backward asymmetric photoelectron energy along the laser propagation direction. By employing nondipole modified strong-field approximation, we attribute this emission-direction-dependent photoelectron energy to the displacement induced by the magnetic component of a laser pulse. The displacement induced by the magnetic field gives rise to a phase difference between the electron wave packets with different ionization instants. It results in a shift of the interference fringes, manifesting as the asymmetric photoelectron energy along the laser propagation direction. By numerically solving the time-dependent Schrödinger equation, we demonstrate that the time-resolved displacement with picometer resolution is traced from the time-delay-dependent asymmetric photoelectron energy in attosecond photoelectron interferometry. The cycle-averaged displacement is retrieved from the intercycle interference and dynamic interference. Moreover, we show that the magnetic field induced momentum also results in emission-direction-dependent photoelectron energy. From the asymmetric photoelectron energy in the attosecond streaking spectrum, the time-resolved momentum induced by the magnetic field is revealed.

I. INTRODUCTION

Photoionization is one of the most fundamental processes in laser-matter interactions and has served as a powerful tool to study the structure and dynamics of matters. In the theoretical description of photoionization, electric dipole approximation is widely used, in which the spatial dependence of the light electric field and the magnetic-field component are both ignored. It usually holds well for the most commonly used near-infrared laser sources and intensities, while in the short-wavelength regime and high-intensity long-wavelength limit [1], the nondipole effect is nonnegligible.

Recently, with advances in detecting technologies, the nondipole effect has become observable and aroused considerable interest. In the short-wavelength regime, such as ionization by x-ray, the electric-quadrupole effect is significant. It manifests as an asymmetric photoelectron angular distribution along the laser propagation direction [2–5]. This nondipole effect is significantly enhanced in autoionization [6], Cooper minimum [7], as well as multiphoton resonant [8]. In the high-intensity long-wavelength limit, the magnetic-field effect is nonnegligible. For example, in strong-field ionization by IR field, the magnetic field complicates the electron-ion partition of photon linear momenta [9–16] and significantly alters the laser-induced electron-ion rescattering process [17–27] (see Refs. [28,29] for recent review).

Moreover, the nondipole effect also results in forward-backward asymmetric photoelectron energy along the laser propagation direction. This effect has been observed in above-threshold ionization (ATI) [30–32] and ionization by intense high-frequency laser pulse in the atomic stabilization regime [33], where it was shown that the electron emitted against the laser propagation direction acquires larger energy than that emitted along the laser propagation direction. When the energy shift becomes comparable to the photon energy or the energy interval of the interference peaks, this emission-direction-dependent photoelectron energy induces the disappearance of the ATI peaks [34] or the dynamic interference structure [33,35,36] in the photoelectron energy spectrum. In these works, this emission-direction-dependent photoelectron energy is attributed to the nondipole modified Stark shift of continued states, i.e., the photoelectron-momentum-dependent ponderomotive energy $U_{\text{eff}} = (1 + p_y/c)U_p$ [30,33,37,38]. Here, p_y is the electron momentum along the light propagation direction, U_p is the ponderomotive energy of the laser pulse, and c is the light speed. Since the ponderomotive energy is a cycle-averaged concept, this picture is only suitable for static studies on the nondipole effect as addressed in the above-mentioned works. A more interesting issue is the time-resolved nondipole photoelectron dynamics driven by the laser pulse. It provides the information of the instantaneous nondipole effect on photoelectrons. In recent years, numerous attosecond metrologies have been developed to deliver real-time information on electronic processes in ultrafast time scales [39–46], but most of them are built up by the electric dipole approximation. How

*lbguo@hust.edu.cn
†zhouymhust@hust.edu.cn

to use these techniques to time resolve the nondipole electron dynamic is still an open question.

In this work, we aim at revealing the time-resolved electronic motion driven by the magnetic component of the laser field from the emission-direction-dependent photoelectron energy. By employing strong field approximation with nondipole correction, we attribute this forward-backward photoelectron energy shift to the displacement induced by the magnetic component of Lorenz force. The magnetic-field-induced displacement results in a p_y-dependent phase for the electronic wave packets (EWPs) emitted at different instants. Here, p_y is the electron momentum along the light propagation direction. This p_y-dependent phase difference results in a photoelectron interference fringes shift along the laser propagation direction, manifesting as the emission-direction-dependent photoelectron energy. By numerically solving the time-dependent Schrödinger equation (TDSE), we demonstrate that the displacement induced by the magnetic field can be traced from this asymmetric photoelectron energy along the laser propagation direction. Specifically, the time-resolved magnetic-field-induced displacement is revealed by attosecond photoelectron interferometry with picometer resolution, and the cycle-averaged displacement is revealed by intercycle interference and dynamic interference. Moreover, the photoelectron momentum induced by the magnetic field distorts the photoelectron momentum distribution, which also manifests as the forward-backward asymmetric photoelectron energy shift. The time-resolved momentum resulting from the magnetic field is revealed by the attosecond streaking technique.

This article is organized as follows. In Sec. II, we introduce our method for numerically solving the three-dimensional (3D) TDSE beyond the dipole approximation and the nondipole effect modified strong-field approximation (ndSFA). In Sec. III A, we demonstrate that the static displacement induced by the magnetic field effect can be revealed from intercycle interference and dynamic interference. In Secs. III B and III C, the time-resolved displacement and momentum induced by the magnetic field are traced by attosecond photoelectron interferometry and the attosecond streaking technique, respectively. Section IV provides a brief summary.

II. THEORY AND METHODOLOGY

A. Numerically solving TDSE

The dynamics of an atom interacting with the laser pulses are governed by the TDSE, in which the Hamiltonian including nondipole corrections to the first order in $1/c$ is given by (atomic units are used unless otherwise stated) [15,47–49]

$$H = \frac{1}{2}\left[\mathbf{p} + \mathbf{A}(t) + \frac{\mathbf{e}_y}{c}\left(\mathbf{p}\cdot\mathbf{A}(t) + \frac{1}{2}\mathbf{A}^2(t)\right)\right]^2$$
$$+ V\left(\mathbf{r} - \frac{y}{c}\mathbf{A}(t)\right), \tag{1}$$

where $\mathbf{A}(t) = \mathbf{A}(t, y = 0)$ is the laser vector potential at the position of the nucleus. In our calculation, the laser field is polarized in the *x-z* panel and propagates along the *y* axis. $V(\mathbf{r}) = -1/r$ is the Coulomb potential of the H atom. To speed up the time propagation, we expand the shifted potential

to first order in $1/c$, i.e. [47],

$$V\left(\mathbf{r} - \frac{y}{c}\mathbf{A}(t)\right) \approx V(\mathbf{r}) - \frac{y}{c}\mathbf{A}(t)\cdot\nabla V(\mathbf{r}). \tag{2}$$

Then, the Hamiltonian in Eq. (1) is reduced to

$$H = \frac{1}{2}\mathbf{p}^2 + \mathbf{p}\cdot\mathbf{A}(t) + \frac{1}{c}p_y\left(\mathbf{p}\cdot\mathbf{A}(t) + \frac{1}{2}\mathbf{A}^2(t)\right)$$
$$- \frac{1}{r} - \frac{y}{c}\mathbf{A}(t)\cdot\frac{\mathbf{r}}{r^3}. \tag{3}$$

Note that here the purely time-dependent quadratic $\frac{1}{2}\mathbf{A}^2(t)$ term has been removed by the gauge transformation

$$\Psi' = \exp\left[i\int_0^t \frac{1}{2}\mathbf{A}^2(t')dt'\right]\Psi. \tag{4}$$

In our simulation, the TDSE with the Hamiltonian in Eq. (3) is solved in the spherical coordinates, in which the wave function $\Psi(\mathbf{r}, t)$ is expanded by spherical harmonics $|l, m\rangle$,

$$|\Psi(\mathbf{r}, t)\rangle = \sum_{l,m} \frac{R_{l,m}(r, t)}{r}|l, m\rangle, \tag{5}$$

where $R_{l,m}(r, t)$ is the radial part of the wave function. This radial wave function is discretized by the finite-element discrete variable representation (FE-DVR) method [50–53]. The angular quantum number l and magnetic quantum number m are chosen up to 100 and 20, respectively. The time propagation of the TDSE is calculated by the split-Lanczos method with the time step fixed at $\Delta t = 0.01$ a.u.. The maximal box size for the radial coordinate is chosen to be 200 a.u.. An absorbing function has been applied in each step of time propagation of the wave function, which is written as $F(r) = 1 - 1/(1 + e^{(r-R_c)/L})$ with $R_c = 150$ a.u. and $L = 2$ a.u.. The wave function $\Psi(\mathbf{r}, t)$ is split into the inner part $\Psi_{\text{in}}(\mathbf{r}, t) = \Psi(\mathbf{r}, t)F(r)$ and the outer part $\Psi_{\text{out}} = \Psi(\mathbf{r}, t) - \Psi_{\text{in}}(\mathbf{r}, t)$ by the absorbing function. The inner wave function evolves strictly as TDSE, while the outer part Ψ_{out} is propagated by the Coulomb-Volkov propagator [54]. At each time step t_i, $\Psi_{\text{out}}(\mathbf{r}, t_i)$ is projected to the scattering state $\Psi_p(\mathbf{r})$ to obtain the ionization amplitude $\mathcal{M}'(\mathbf{p}, t_i) = \langle \Psi_p(\mathbf{r})|\Psi_{\text{out}}(\mathbf{r}, t_i)\rangle$. Then from time t_i to the next time step $t_{i+1} = t_i + \Delta t$, the ionization continuum is only changed by a Volkov phase with the nondipole correction [13,30,55]

$$U_{\mathbf{p}}(t_i, t_{i+1}) = \exp\left\{-i\int_{t_i}^{t_{i+1}}\left[\frac{p^2}{2} + \mathbf{p}\cdot\mathbf{A}(\tau)\right.\right.$$
$$\left.\left. + \frac{p_y}{c}\left(\mathbf{p}\cdot\mathbf{A}(\tau) + \frac{\mathbf{A}^2(\tau)}{2}\right)\right]d\tau\right\}. \tag{6}$$

At time t_{i+1}, we add the amplitude propagated from t_i and the new splitting amplitude $\mathcal{M}'(\mathbf{p}, t_{i+1})$,

$$\mathcal{M}(\mathbf{p}, t_{i+1}) = U_{\mathbf{p}}(t_i, t_{i+1})\mathcal{M}(\mathbf{p}, t_i) + \mathcal{M}'(\mathbf{p}, t_{i+1}). \tag{7}$$

Note that we use $\mathcal{M}'$ to indicate the new splitting amplitude from the TDSE calculation and $\mathcal{M}$ to indicate the sum of all amplitudes, including the new splitting one and those propagated from the previous splitting times. At the end time t_f of the propagation, splitting is not needed anymore and the new

produced amplitude $\mathcal{M}'(\mathbf{p}, t_f)$ is extracted from the whole wave function $\Psi(\mathbf{r}, t_f)$ at time t_f. Adding all the amplitudes at time t_f, we obtain the final ionization amplitude $\mathcal{M}(\mathbf{p}, t_f)$. Then the photoelectron momentum distributions (PEMDs) are given by

$$\mathcal{P}(\mathbf{p}) = |\mathcal{M}(\mathbf{p}, t_f)|^2. \qquad (8)$$

In our work, $\Psi_p(\mathbf{r})$ is chosen as the scattering state of the H atom [56], which is normalized by $\int d\mathbf{r}\Psi_p^*(\mathbf{r})\Psi_{p'}(\mathbf{r}) = \delta(\boldsymbol{p} - \boldsymbol{p}')$. The convergence of our calculations has been confirmed by changing l, m, and R_c in our calculations. The initial wave function is prepared by the imaginary-time propagation, which is chosen as the ground state of the H atom.

B. Nondipole effect modified strong-field approximation

Neglecting the Coulomb potential in Eq. (1), the Volkov state (eigenstate of potential-free Hamiltonian) with the nondipole effect correction can be written as [30,55]

$$\left|\psi_{\mathbf{p}}^V(t)\right\rangle = e^{-iS(\mathbf{p},t)}|\mathbf{p}\rangle = e^{-\int^t \mathbf{k}^2(t')/2dt'}|\mathbf{p}\rangle, \qquad (9)$$

consisting of plane waves $|\mathbf{p}\rangle$ and the generalized action $S(\mathbf{p}, t) = \int^t \mathbf{k}^2(t')/2dt'$. $\mathbf{k}(t')$ is the kinetic momentum of the electron with a canonical momentum $\mathbf{p}$ in the laser field

$$\mathbf{k}(t') = \mathbf{p} + \mathbf{A}(t') + \frac{\mathbf{e}_y}{c}\left[\mathbf{p} \cdot \mathbf{A}(t') + \frac{1}{2}\mathbf{A}^2(t')\right]. \qquad (10)$$

This expression of the electron kinetic momentum is the same as is given by the Newton equation $d\mathbf{k}(t)/dt = \mathbf{E}(t) + \mathbf{k}(t) \times \mathbf{B}(t)$. Here, $\mathbf{E}(t) = -d\mathbf{A}(t)/dt$ and $\mathbf{B}(t) = -d\mathbf{A}(t)/dt/c$ are the electric and magnetic field effect, respectively. Thus, the additional term [last term in Eq. (10)] is induced by the magnetic component of the laser field, which drives the electron along the laser propagation direction. In Sec. III C, we will show that the time-resolved momentum induced by the magnetic field can be traced from the forward-backward asymmetric photoelectron energy along the laser propagation direction in the attosecond streaking.

Furthermore, from Eq. (10), the displacement of the photoelectron with ionization time t_0 in the laser field is given by

$$\mathbf{r}(t) = \mathbf{p}(t - t_0) + \int_{t_0}^t \mathbf{A}(t')dt'$$
$$+ \frac{\mathbf{e}_y}{c}\int_{t_0}^t\left[\mathbf{p} \cdot \mathbf{A}(t') + \frac{1}{2}\mathbf{A}^2(t')\right]dt'$$
$$= \mathbf{p}(t - t_0) + \boldsymbol{\alpha}_{\mathrm{E}}(t) + \alpha_{\mathrm{M}}(t)\mathbf{e}_y, \qquad (11)$$

where the first term represents the free propagation of the photoelectron, and $\boldsymbol{\alpha}_{\mathrm{E}}(t)$ and $\alpha_{\mathrm{M}}(t)$ are the displacement induced by the electric and magnetic field, respectively. Then, as indicated by Eq. (9), the phase difference for interference of the two EWPs emitted at t_1 and t_2 is given by

$$\Delta S = S(\mathbf{p}, t_1) - S(\mathbf{p}, t_2) + \Delta\phi$$
$$= \frac{\mathbf{p}^2}{2}\Delta t + \mathbf{p} \cdot \Delta\boldsymbol{\alpha}_{\mathrm{E}} + p_y\Delta\alpha_{\mathrm{M}} + \Delta\phi. \qquad (12)$$

Here, $\Delta\phi$ is the momentum-independent phase difference, which depends on the ionization regime. $\Delta t = t_1 - t_2$, $\Delta\boldsymbol{\alpha}_{\mathrm{E}} = \boldsymbol{\alpha}_{\mathrm{E}}(t_2) - \boldsymbol{\alpha}_{\mathrm{E}}(t_1)$ and $\Delta\alpha_{\mathrm{M}} = \alpha_{\mathrm{M}}(t_2) - \alpha_{\mathrm{M}}(t_1)$ are the
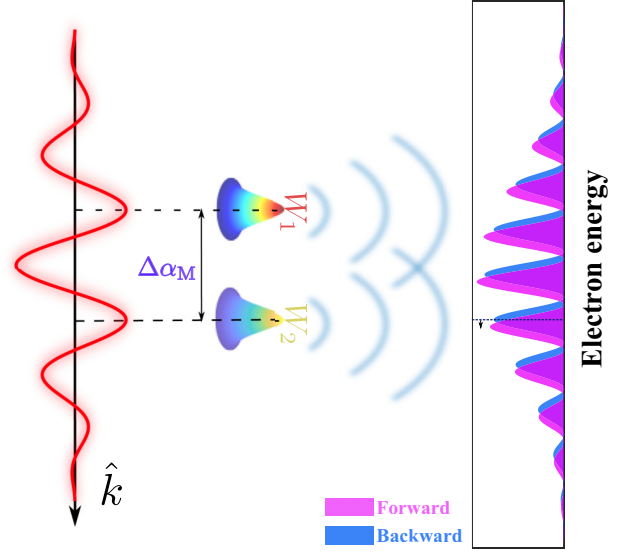

FIG. 1. Schematic illustration of the manifestation of the displacement induced by the magnetic field on photoelectron interference. Under the influence of the magnetic field of a laser pulse, the two EWPs with different ionization instants have a displacement difference, $\Delta\alpha_{\mathrm{M}}$. This displacement gives rise to the phase difference between the two EWPs, which results in the shift of the interference fringes along the light propagation. By extracting the shift of the interference fringes, the magnetic-field-induced displacement can be revealed. $\hat{k}$ represents the laser propagation direction.

displacement difference induced by the electric field and magnetic field, respectively. Within the dipole approximation, $\Delta\alpha_{\mathrm{M}}$ disappears and thus the phase ΔS is exactly symmetric about $p_y = 0$. The third term in Eq. (12) leads to the forward-backward asymmetry in the phase distribution. This asymmetric phase results in the energy shift of the interference fringes along the laser propagation direction, i.e., emission-direction-dependent photoelectron energy. Figure 1 illustrates this magnetic field effect on the interference fringes. The two EWPs have different magnetic-field-induced displacements due to their different ionization instants. This displacement difference gives rise to a momentum-dependent phase difference between two EWPs, $p_y\Delta\alpha_{\mathrm{M}}$, which results in the shift of the interference fringes along the light propagation. It means that the magnetic-field induced displacement can be retrieved from this interference fringes shift. We should mention that the magnetic-field induced displacement is usually in the picometer scale. In the following, we will show how to trace such tiny displacement from the photoelectron interference.

In this work, we focus on the PEMD in the p_y-p_z plane ($p_x = 0$) and analyze the interference fringes at polar coordinates, i.e., $p_z = p_r \cos\theta$ and $p_y = p_r \sin\theta$. Then, as indicated by Eq. (12), the peak position of the interference fringes for the forward ($p_y > 0$, $\theta > 0$) and backward ($p_y < 0$, $\theta < 0$) is determined by

$$\frac{p_r^{+2}}{2}\Delta t + p_r^+ \cos\theta \Delta\alpha_{\mathrm{E}} + p_r^+|\sin\theta|\Delta\alpha_{\mathrm{M}} + \Delta\phi = 2n\pi$$

$$\frac{p_r^{-2}}{2}\Delta t + p_r^- \cos\theta \Delta\alpha_{\mathrm{E}} - p_r^-|\sin\theta|\Delta\alpha_{\mathrm{M}} + \Delta\phi = 2n\pi.$$
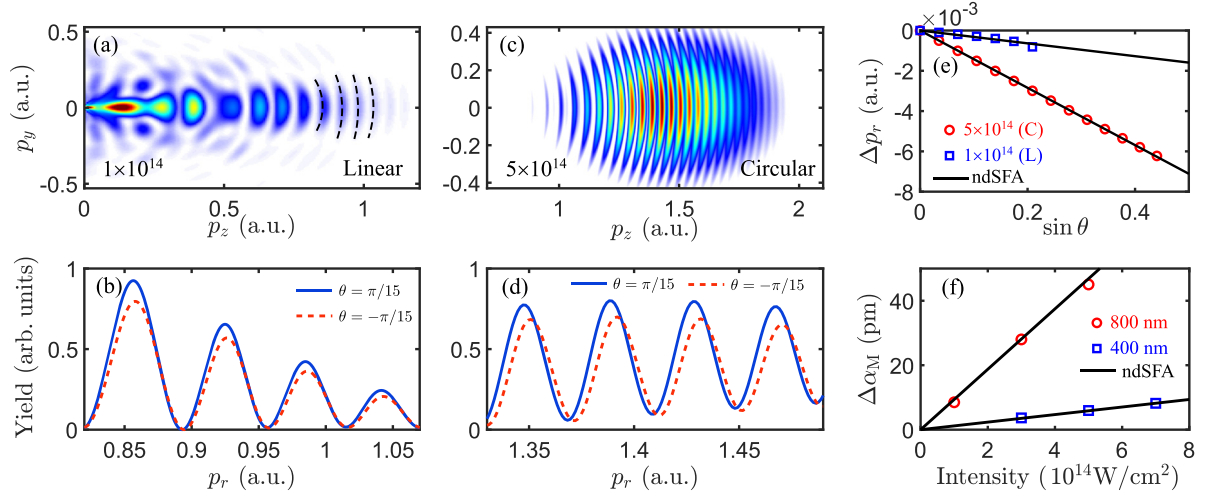$$(13)$$

FIG. 2. (a) TDSE results of PEMD in (p_y, p_z) plane from ionization of H atom by a linearly polarized IR pulse with wavelength of 800 nm, intensity of 1×10^{14} W/cm^2 and a $\sin^2$ envelope lasting five cycles. The black dashed lines mark the ATI peaks. (b) Cuts of the PEMD at $\theta = \pi/15$ (blue solid line) and $\theta = -\pi/15$ (red dashed line). (c and d) The same as (a) and (b) but for the circularly polarized IR field with the intensity of 5×10^{14} W/cm^2. (e) Comparison of the momentum shift of the interference fringes Δp_r extracted from the TDSE results (symbols) and predicted by ndSFA (solid lines). The red circles and blue squares represent extracted results from (a) and (c), respectively. (f) Comparison of the magnetic-field-induced displacement extracted from the TDSE results (symbols) and predicted by ndSFA (solid lines). The red circles and blue squares represent the results for circularly polarized laser pulses with wavelengths of 800 nm and 400 nm, respectively.

Here, n is an integer number, and the superscripts $\pm$ indicate the forward and backward electrons, respectively. Then, we have

$$\Delta p_r = p_r^+ - p_r^- = -2\Delta\alpha_{\mathrm{M}} \sin\theta / \Delta t. \quad (14)$$

This equation shows that the energy shift directly relates to the displacement induced by the magnetic field. It means that the electron motion driving by the magnetic field can be traced by this emission-direction-dependent photoelectron energy.

III. RESULTS AND DISCUSSION

In this section we present our numerical results to demonstrate the scheme addressed in Sec. II B. Firstly, we show that the cycle-averaged displacement induced by the magnetic field is revealed from the intercycle interference and dynamic interference. More importantly, the subcycle time-resolved displacement and momentum induced by the magnetic field is traced from attosecond photoelectron interferometry and the attosecond streaking technique, respectively.

A. Tracing cycle-averaged displacement induced by magnetic field

Figure 2(a) displays the TDSE results of PEMD in the p_y-p_z plane ($p_x = 0$) from ionization of an H atom by a linearly polarized IR field with a wavelength of 800 nm and intensity of 1×10^{14} W/cm^2. The interference structures marked by the black dashed lines in Fig. 2(a) are the ATI rings, which originate from the EWPs emitted at adjacent laser cycles, i.e., intercycle interference. To show PEMD asymmetry along the laser propagation direction induced by the nondipole effect, the cuts of the PEMD at $\theta = \pi/15$ (forward) and $\theta = -\pi/15$ (backward) are displayed in Fig. 2(b). With the dipole approximation, the PEMD at $\theta = \pm\pi/15$ is exactly the same,

while within the nondipole effect, in addition to the asymmetric yield of PEMD, the energy of the interference peaks for $\theta = -\pi/15$ is larger than for $\theta = \pi/15$. In this work, we focus on this magnetic field effect induced forward-backward energy shift of the interference structure. The TDSE results for a more intense (5×10^{14} W/cm^2) circularly polarized laser pulse are shown in Figs. 2(c) and 2(d). The PEMD shows a more significant energy shift.

For this intercycle interference, the time interval of the EWPs equals the period of the laser pulse, i.e., $\Delta t = T_{\mathrm{IR}}$. Then, the displacement difference is given by

$$\Delta\alpha_{\mathrm{M}} = \frac{1}{c} \int_{t_0}^{t_0+T_{\mathrm{IR}}} \left[\mathbf{p} \cdot \mathbf{A}(t') + \frac{1}{2}\mathbf{A}^2(t') \right] dt'$$

$$= \frac{1}{c} U_p T_{\mathrm{IR}}. \quad (15)$$

Here, $U_p = A_0^2/4$ is the ponderomotive energy of the laser pulse, and A_0 is the amplitude of the vector potential of the IR field. Note that the oscillation of the term $\mathbf{A}(t')$ and $\mathbf{A}^2(t')$ is smoothed out by cycle average. Then, as indicated by Eq. (14), the interference fringe shift is given by

$$\Delta p_r = -\frac{2U_p}{c} \sin\theta. \quad (16)$$

This formula is the same as the results given by the previous works [30,37,38], in which the energy shift is attributed to the nondipole effect modified Stark shift of the continued state. The fringe shift extracted from the TDSE results of PEMD is displayed by the symbols in Fig. 2(e), which agrees well with the prediction by the ndSFA model as shown by the black solid lines. This agreement indicates that the energy shift of this intercycle interference in the high-energy region (8~12 eV) is not affected by the Coulomb interaction during and after tunneling and disturbance of various types of
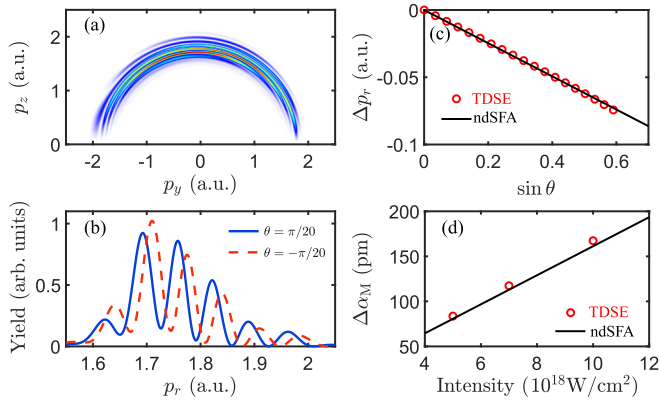
FIG. 3. TDSE results of PEMD from ionization of H atom by an XUV laser pulse with the center frequency of $\omega = 2$ a.u., intensity of 1×10^{19} W/cm^2, and a Gaussian envelope with FWHM of seven cycles. (b) Cuts of the PEMD at $\theta = \pi/20$ (blue solid line) and $\theta = -\pi/20$ (red dashed line). (c) Comparison of the momentum shift of the interference fringes Δp_r extracted from the TDSE results (symbols) and predicted by ndSFA (solid lines). (d) Comparison of the magnetic-field-induced displacement extracted from the TDSE results (symbols) and predicted by ndSFA (solid lines) for different laser intensities.

interference in the linearly polarized laser pulse. The deviation between the experimental results and the ndSFA model shown in previous work [32] may come from the imperfect detection of the experimental setup. More importantly, the displacement can be traced by linearly fitting the fringe shift as a function of $\sin \theta$ whose slope equals $-2\Delta\alpha_M/T_{IR}$. The retrieved displacements for different intensities and wavelengths are displayed by the symbols in Fig. 2(f). The ndSFA prediction given by Eq. (15) is also shown by the solid lines for comparison. These results agree well with each other. The magnetic-field-induced displacement accumulated in a laser cycle is about several tens of picometers for the laser parameters considered in our work. Furthermore, this displacement is larger in the longer-wavelength laser pulse, which coincides with our understanding of the onset of the magnetic field effect in long-wavelength limit.

In addition to the long-wavelength limit, the magnetic-field effect is also observable in the intense extreme ultraviolet (XUV) laser field. In past decades, numerous counterintuitive phenomena induced by the magnetic-field effect in the atomic stabilization regime have been investigated [51,57–61]. Here, we focus on the magnetic-field effect in dynamic interference. Figure 3(a) displays the TDSE results of the PEMD from ionization of an H atom by an XUV pulse with the center frequency of $\omega = 2$ a.u., intensity of 1×10^{19} W/cm^2, and a Gaussian envelope with a full width at half maximum (FWHM) of seven cycles. The ring-like structure originates from the single-photon ionization, and the modulations on the ring-like structures originate from the dynamic interference [52,62–65]. With the dipole approximation, the PEMD should be symmetric about $p_y = 0$, while with the nondipole effect, this PEMD shows significant asymmetry, which is induced by the magnetic field of such an intense laser field. The cuts of the PEMD at $\theta = \pi/20$ (forward) and $\theta = -\pi/20$ (backward) are shown in Fig. 3(b) by the blue solid and red dashed

lines, respectively. Similar to the intercycle interference, there is a significant negative energy shift between the forward-backward photoelectron emission.

The dynamic interference originates from the interference of the EWPs emitted at the rising and falling edge of the laser pulse. The exact emitting time points of the EWPs generated at rising edge (t_1) and falling edge (t_2) could be determined by the stationary-phase approximation of the electron dynamic phase [62], while for present laser pulses with such high intensities, the time points of the dominated ejection are located close to the tails of the laser pulse due to the atomic stabilization, i.e., $t_1 \approx 0$ and $t_2 \approx T$. In our calculation, the laser pulse starts at 0, and T is the pulse duration of the laser field. Therefore, the magnetic-field-induced displacement between these two EWPs is given by

$$\Delta\alpha_M = \frac{1}{c}\int_0^T \frac{1}{2}\mathbf{A}^2(t')dt'. \tag{17}$$

Note that the first term of displacement, $\mathbf{p} \cdot \mathbf{A}(t)$ in Eq. (15), vanishes because the time average of $\mathbf{A}(t)$ is zero. Then, the interference fringes shift is written as

$$\Delta p_r = -\frac{1}{c}\frac{1}{T}\int_0^T \mathbf{A}^2(t')dt' \sin\theta. \tag{18}$$

Figure 3(c) displays the comparison between the momentum shift extracted from the PEMD and the prediction by the ndSFA. It shows that these results agree well with each other. The retrieved magnetic-field-induced displacement as a function of the laser intensity is displayed in Fig. 3(d), which agrees well with the ndSFA. In this case, the magnetic-field-induced displacement is about several hundred picometers. Since the time interval of the EWP emission for dynamic interference approximately equals the pulse duration, the displacement induced by the entire laser pulse is traced. In this section, we demonstrate that the magnetic-field-induced displacements accumulated in a laser cycle and the entire laser pulse can be traced by intercycle interference and dynamic interference, respectively. However, the time-resolved information of the electron dynamics driven by the magnetic field is absent in these interference. In the following, we will show how to trace the time-resolved magnetic-field-induced electron motion.

B. Time resolving the magnetic-field-induced displacement by attosecond photoelectron interferometry

Here, we employ attosecond photoelectron interferometry, which is based on single-photon ionization in the combination of a phase-locked IR field and two weak XUV pulses separated by the half-cycle of the IR pulse, to trace the time-resolved displacements induced by the magnetic field of the IR pulse. This interferometry has been experimentally observed in different targets [39,40]. It has been widely used to reconstruct the wave functions of atoms and molecules [39], monitor coherent electron scattering [40], characterize the laser pulses [66], etc.

In attosecond photoelectron interferometry, the nondipole effects of the weak XUV pulses and IR field both result in the asymmetric PEMD along the laser propagation direction. Let us first consider the nondipole effect of the weak XUV
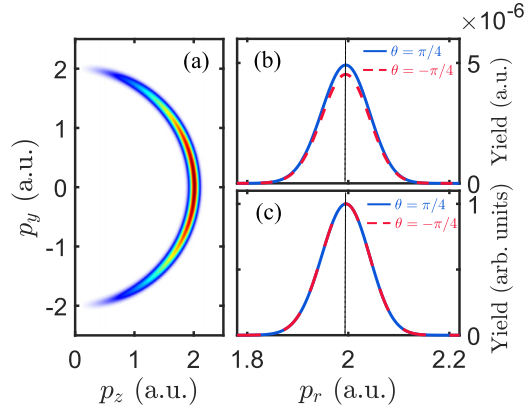
FIG. 4. (a) TDSE results of PEMD in the (p_y, p_z) plane from single-photon ionization in an XUV pulse with the center frequency of $\omega = 2.5$ a.u., intensity of 1×10^{13} W/cm^2, and a Gaussian envelope with FWHM of five cycles. (b) Cuts of the PEMD $\theta = \pi/4$ (blue solid line) and $\theta = -\pi/4$ (red dashed line). (c) Normalized PEMD by their maxima. The colors of lines correspond to the colors in (b).

pulses. The PEMD from ionization by a linearly polarized XUV pulse with the center frequency of $\omega_{\mathrm{XUV}} = 2.5$ a.u. and intensity of 1×10^{13} W/cm^2 is displayed in Fig. 4(a). The cuts of the PEMD at $\theta = \pm\pi/4$ are displayed in Fig. 4(b). It shows that the yields of the PEMDs are asymmetric, which originates from the electric quadrupole effect. The normalized PEMDs by their maxima are shown in Fig. 4(c). No momentum shift is observed for ionization by XUV pulse alone. It indicates that the nondipole effect of such a weak XUV pulse does not affect the momentum shift we focused on in this work.

Figure 5(b) displays the TDSE results of PEMDs at $\theta = \pm\pi/6$ for ionization by the combination of the XUV and

IR field with the time delay $\tau = -T_{\mathrm{IR}}/4$. The corresponding vector potential of the laser pulse is shown in Fig. 5(a), in which the wavelength and intensity of the IR field is 1600 nm and 1×10^{13} W/cm^2, and the laser parameters for the XUV pulse are the same as those in Fig. 4. Similar to the intercycle interference and dynamic interference, the interference fringes reveal a negative momentum shift between the forward and backward emission direction. This momentum shift originates from the magnetic field effect of the IR field. More interestingly, for the time delay $\tau = T_{\mathrm{IR}}/4$, as shown by Figs. 5(c) and 5(d), the PEMD reveals a positive momentum shift. It means that the electron emitted against the laser propagation direction acquires smaller energy than that emitted along the laser propagation direction. This positive momentum shift has not been observed in previous works. It is greatly different from the above static studies. This time-delay-dependent momentum shift originates from the time-delay-dependent displacements induced by the magnetic field. As indicated by Eq. (11), for the IR field with the vector potential $\mathbf{A}_{\mathrm{IR}}(t) = A_0 \cos(\omega_{\mathrm{IR}} t)\hat{e}_z$, the displacement $\Delta\alpha_{\mathrm{M}}(\tau)$ for attosecond photoelectron interferometry is given by

$$\Delta\alpha_{\mathrm{M}}(\tau) = \frac{1}{c} \int_{\tau}^{\tau + T_{\mathrm{IR}}/2} \left[\mathbf{p} \cdot \mathbf{A}(t') + \frac{1}{2}\mathbf{A}^2(t') \right] dt'$$
$$= \frac{T_{\mathrm{IR}}}{c} \left(\frac{1}{\pi} p_z A_0 \sin(\omega_{\mathrm{IR}}\tau) + \frac{1}{2}U_p \right). \quad (19)$$

It shows that the time-delay dependence of displacement is induced by the term of $\mathbf{p} \cdot \mathbf{A}(t)$, which originates from the momentum-dependent magnetic component of Lorenz force. In the intercycle interference and dynamic interference, this term vanishes because the time average of $\mathbf{A}(t)$ is zero. Then, the time-delay-dependent momentum shift is
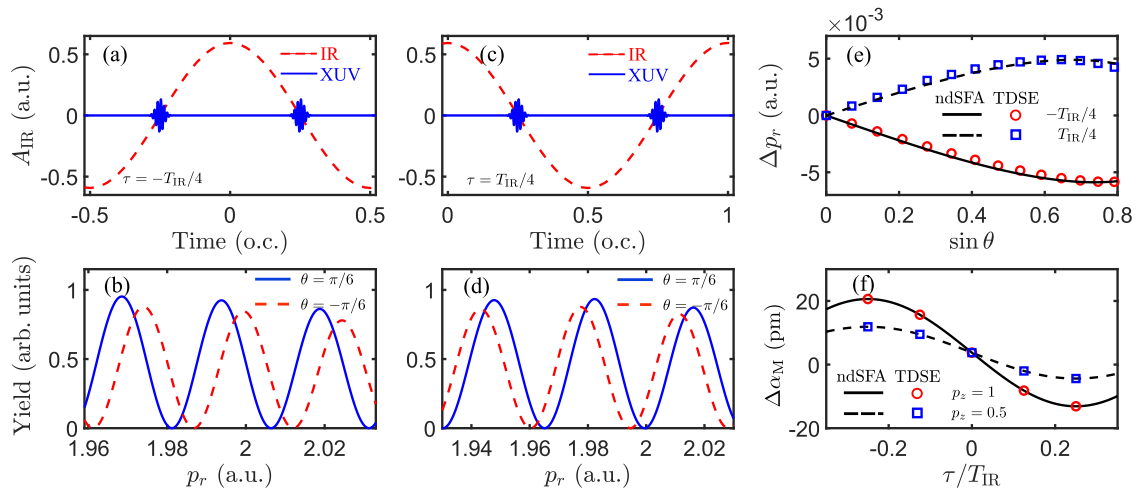

FIG. 5. (a) Vector potentials of the combination of the two XUV pulses and IR field with time delay of $\tau = -T_{\mathrm{IR}}/4$. The red and blue lines represent the vector potential of the XUV pulse and IR field, respectively. The wavelength and the intensity of the IR field are 1600 nm and 1×10^{13} W/cm^2. The center frequency of the XUV pulse is $\omega_{\mathrm{XUV}} = 2.5$ a.u., and its intensity is 1×10^{13} W/cm^2. (b) Cuts of the PEMD $\theta = \pi/6$ (blue solid line) and $\theta = -\pi/6$ (red dashed line) for the ionization in the laser field shown in (a). (c and d) The same as (a) and (b) but for the time delay of $\tau = T_{\mathrm{IR}}/4$. (e) Comparison of the momentum shift of the interference fringes Δp_r extracted from the TDSE results (symbols) and predicted by ndSFA (black lines). The red circles and blue squares represent results for $\tau = -T_{\mathrm{IR}}/4$ and $\tau = T_{\mathrm{IR}}/4$, respectively. (f) Time-resolved magnetic-field-induced displacement. The symbols and lines represent the TDSE and ndSFA results, respectively.

given by

$$\Delta p_r(\tau) = -\frac{4}{c}\left[\frac{1}{\pi}p_z A_0 \sin(\omega_{IR}\tau) + \frac{1}{2}U_p\right]\sin\theta$$

$$= -\frac{4}{c}\left[\frac{1}{\pi}p_r\cos\theta A_0 \sin(\omega_{IR}\tau) + \frac{1}{2}U_p\right]\sin\theta. \quad (20)$$

The momentum shifts as a function of $\sin\theta$ extracted from the PEMD are displaced in Fig. 5(e), in which the blue square and red circle represents the results for $\tau = T_{IR}/4$ and $\tau = -T_{IR}/4$, respectively. This result agrees well with the ndSFA prediction. This momentum shift is not linearly dependent on $\sin\theta$ anymore due to the p_z-dependent displacement induced by the magnetic field. In this case, the displacement is retrieved by $\Delta\alpha_M(\tau) = -\Delta p_r(\tau)T_{IR}/4\sin\theta$, and the retrieved time-delay-dependent displacement is displayed in Fig. 5(f). The blue squares and red circles represent the results for $p_z = 0.5$ and $p_z = 1$, respectively. This displacement oscillates with the time delay around the average value $U_p T_{IR}/2c$. Note that the displacement difference is not always along the laser propagation direction. It depends on the electron ionization instant. It means that the magnetic component of Lorenz force acting on the photoelectron is not always along the laser propagation direction. For some ionization instants and larger momentum of photoelectron, the displacement induced by the magnetic field is against the laser propagation direction, which causes the positive momentum shift between the forward and backward photoelectrons shown in Fig. 5(d). This cannot be revealed in static measurements.

So far, we have demonstrated that the subcycle time-resolved magnetic-field-induced displacements can be traced from the forward-backward interference fringe shift with picometer resolution. The manifestation of this nondipole effect in attosecond photoelectron interferometry reveals a great difference from the intercycle and dynamic interferences. The photoelectron energy peak shift is not always against the laser propagation direction. It depends on the ionization instant and photoelectron momentum.

C. Time resolving the magnetic-field-induced momentum by attosecond streaking technique

In addition to the magnetic-field-induced displacement, the momentum induced by the magnetic field also results in emission-direction-dependent photoelectron energy. In this section, we will demonstrate this scheme by the attosecond streaking technique. The attosecond streaking, which is based on an attosecond XUV pulse serving as the pump pulse and a phase-controlled IR field as the probe pulse, is also capable of delivering real-time information on electronic processes in ultrafast time scales [41,42,67].

Figure 6(a) displays the TDSE results of PEMD in the (p_y, p_z) plane (i.e., $p_x = 0$) with $\tau = -T_{IR}/4$. The inset shows the corresponding vector potential of the IR pulse and the red circle marks the time delay between XUV and IR pulse. The wavelength and the intensity of the IR field are 3600 nm and 5×10^{12} W/cm^2. The laser parameters for XUV are the same as those in Fig. 5. The PEMD shows a ring-like structure with two half-rings located at the $p_z > 0$ and $p_z < 0$ plane denoted by peak1 and peak2, respectively. The cuts of the PEMDs at
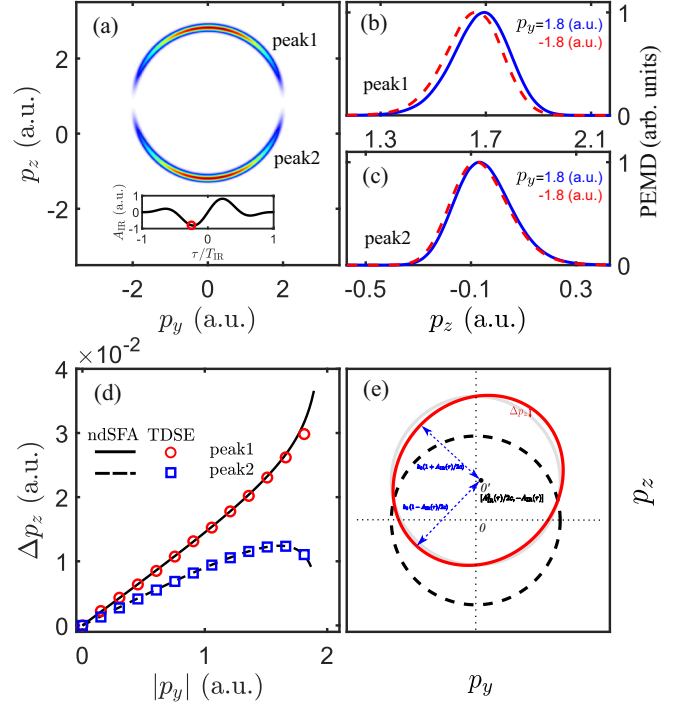

FIG. 6. (a) TDSE results of PEMD in the (p_y, p_z) plane from single-photon ionization in the combination of single XUV pulses and IR field. The inset shows the vector potential of the IR pulse and the red circle marks the time delay between XUV and IR pulse. The wavelength and the intensity of the IR field are 3600 nm and 5×10^{12} W/cm^2. The laser parameters for XUV are the same as those in Fig. 4. (b and c) Cuts of the PEMD at $|p_y| = 1.8$. Note that the cuts are normalized by their maxima. The top and bottom rows display the PEMDs corresponding to peak1 and peak2, respectively. (d) Momentum shift as a function of $|p_y|$. The symbols and lines represent the TDSE and ndSFA results, respectively. The red circles and blue squares are the results for peak1 and peak2 shown in (a), respectively. (e) Schematic illustration of the effect of magnetic field of the IR field on the PEMDs. The black solid line represents the PEMD from single-photon ionization in the XUV pulse alone. It is a ring centered at $[p_y, p_z] = [0, 0]$ with the radius of k_0. The red solid line represents the PEMD in the XUV-IR pulse with nondipole correction determined by Eq. (22). It is a ellipse centered at $[p_y, p_z] = [A_{IR}^2(\tau)/2c, -A_{IR}(\tau)]$ with major and minor axes $k_0[1 - A_{IR}(\tau)/2c]$ and $k_0[1 + A_{IR}(\tau)/2c]$, respectively. The PEMD with the dipole approximation is also displayed by the gray solid line for comparison, which is a ring centered at $[0, -A_{IR}(\tau)]$.

$p_y = \pm 1.8$ a.u. are displayed in Figs. 6(b) and 6(c). Note that the cuts are normalized by their maxima. It shows that there is a peak shift between the PEMD for $p_y > 0$ and $p_y < 0$. More interestingly, the peak shift of peak1 is much larger than that for peak2.

As indicated by Eq. (10), the momentum in the $p_z - p_y$ panel at the ionization instant τ in the attosecond streaking is given by

$$\mathbf{k}(\tau) = [p_z + A_{IR}(\tau)]\hat{e}_z + \left[p_y + \frac{p_z}{c}A_{IR}(\tau) + \frac{A_{IR}^2(\tau)}{2c}\right]\hat{e}_y. \quad (21)$$
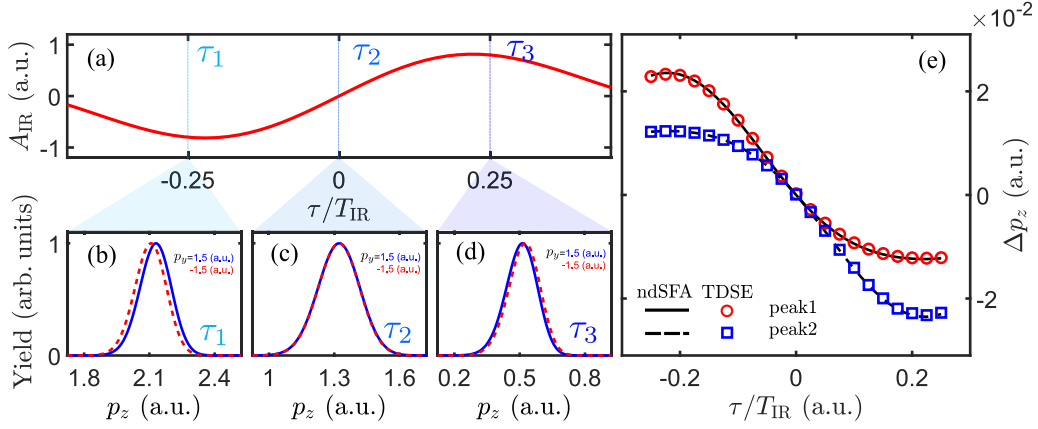
FIG. 7. (a) Vector potential of the IR pulse. (b–d) Cuts of the PEMDs for peak1 at $p_y = 1.5$ (blue solid line) and $p_y = -1.5$ (red dashed line) with $\tau = -0.25T_{IR}$, 0 and $0.25T_{IR}$, respectively. (e) Momentum shift as a function of time delay between the XUV and IR pulse. The symbols and lines represent the TDSE and ndSFA results, respectively.

The last two terms are the momentum induced by the magnetic field. By the conservation law of energy at the ionization time, we have the nondipole effect modified attosecond streaking camera

$$[p_z + A_{IR}(\tau)]^2 + \left[p_y + \frac{p_z}{c}A_{IR}(\tau) + \frac{A_{IR}^2(\tau)}{2c}\right]^2 = k_0^2. \quad (22)$$

Here, $k_0 = \sqrt{2(\omega_{XUV} - I_p)}$, ω_{XUV} is the center frequency of the XUV pulse and I_p represents the ionization potential of atoms. This equation implies that the PEMD is a ellipse centered at $[p_y, p_z] = [A_{IR}^2(\tau)/2c, -A_{IR}(\tau)]$ with major and minor axes $k_0[1 - A_{IR}(\tau)/2c]$ and $k_0[1 + A_{IR}(\tau)/2c]$, as illustrated by the red solid line in Fig. 6(e). It means that the PEMD for the ionization of the XUV pulses shifts along the laser polarized direction with the momentum of $-A_{IR}(\tau)$ within the effect of the electric field of the IR pulse, while within the magnetic-field effect of IR field, the PEMD not only shifts along the laser propagation direction with the momentum of $A_{IR}^2(\tau)/2c$, but also is distorted as an ellipse. This ellipse-type PEMD originates from the momentum induced by the magnetic field as shown by the last two terms in Eq. (22). It is responsible for the counterintuitive peak shift shown in Figs. 6(b) and 6(c).

As indicated by Eq. (22), the forward-backward peak shift for peak1 and peak2 is given by

$$\Delta p_z^+ = -2p_y \frac{[2p_{z0} - A_{IR}(\tau)]A_{IR}(\tau)}{2cp_{z0}},$$

$$\Delta p_z^- = -2p_y \frac{[2p_{z0} + A_{IR}(\tau)]A_{IR}(\tau)}{2cp_{z0}}, \quad (23)$$

respectively. Here, $p_{z0} = \sqrt{k_0^2 - p_y^2}$ represents the initial momentum along the laser polarized direction. It shows that the momentum shift depends on the transverse photoelectrons momentum p_y. To show the momentum-dependent peak shift, we extract the forward-backward peak shift as a function of $|p_y|$ as shown in Fig. 6. The red circles and blue squares are the results for peak1 and peak2, respectively. The black lines are the results predicted by the ndSFA model. The results retrieved from the PEMDs remarkably agree with the ndSFA

prediction. This momentum shift reveals a great difference for peak1 and peak2, and it strongly depends on the transverse photoelectrons momentum. This momentum-dependent peak shift originates from the velocity-dependent Lorentz force, $\mathbf{k}(t) \times \mathbf{B}(t)$. The initial momentum of photoelectrons for peak1 and peak2 have opposite direction, thus the momentum induced by the magnetic field is different for these two peaks. It manifests as the momentum-dependent peak shift shown in Fig. 6.

Moreover, the Lorentz force $\mathbf{k}(t) \times \mathbf{B}(t)$ depends on the instantaneous amplitude of the magnetic field. It results in a time-delay-dependent peak shift, shown in Eq. (23). To show the time-delay-dependent peak shift induced by the magnetic field, the cuts of the PEMDs at $p_y = \pm 1.5$ a.u. for peak1 with various time delays are displayed in Figs. 7(a)–7(d). For $A_{IR}(\tau) < 0$, the forward-backward momentum shift has a positive momentum shift, as displayed in Fig. 7(b). On the contrary, for $A_{IR}(\tau) > 0$, the momentum shift is negative, as shown in Fig. 7(d), while for $A_{IR}(\tau) = 0$, the momentum shift vanishes, as indicated by Fig. 7(c). The peak shift as a function of time delay is shown in Fig. 7(e), where the red circles and blue squares represent the results for peak1 and peak2, respectively. It agrees well with the ndSFA prediction as shown by the black lines. This peak shift and the momentum induced by the magnetic field have a similar time-delay dependence, as shown in Eq. (23) and last two terms in Eq. (21). It indicates that the time-resolved momentum induced by the magnetic field is revealed from the asymmetric photoelectron energy in the attosecond streaking spectrum. We should mention that this time-delay-dependent and momentum-dependent magnetic-field effect cannot be revealed by the static study, and this observable momentum shift cannot be neglected in the interpretation of attosecond time-delay experiments.

IV. CONCLUSION

In conclusion, we attribute the forward-backward asymmetric photoelectron energy along the laser propagation direction, which originates from the nondipole interaction, to the photoelectron motion driven by the magnetic field.

By numerically solving the three-dimensional time-dependent Schrödinger equation, we demonstrated our scheme is suitable for various ionization regimes, including static and time-resolved studies on the nondipole effect. We find that the manifestation of emission-direction-dependent photoelectron energy in time-resolved studies shows a great difference from previous static studies. More importantly, according to our scheme, the time-resolved displacement induced by the magnetic field is successfully traced from the emission-direction-dependent photoelectron energy in the attosecond photoelectron interferometry with picometer resolution. Moreover, the time-resolved momentum induced by the magnetic field is revealed from the asymmetric photoelectron energy in the attosecond streaking spectrum.

In previous works, the emission-direction-dependent photoelectron energy is attributed to the nondipole effect modified Stark shift of continue states. It is only suitable for static study of nondipole effect, such as

the interference structures discussed in Sec. III A, but it cannot explain the time-resolved study, such as attosecond photoelectron interferometry and attosecond streaking. Our work provides a different perspective on understanding emission-direction-dependent photoelectron energy, and our scheme paves a way to trace the time-resolved photoelectron motion driven by the magnetic field. It deepens our understanding of magnetic-field effect in photoionization.

[1] H. R. Reiss, Limits on tunneling theories of strong-field ionization, Phys. Rev. Lett. **101**, 043002 (2008).

[2] M. O. Krause, Photo-ionization of krypton between 300 and 1500 eV. Relative subshell cross sections and angular distributions of photoelectrons, Phys. Rev. **177**, 151 (1969).

[3] F. Wuilleumier and M. O. Krause, Photoionization of neon between 100 and 2000 eV: Single and multiple processes, angular distributions, and subshell cross sections, Phys. Rev. A **10**, 242 (1974).

[4] B. Krässig, M. Jung, D. S. Gemmell, E. P. Kanter, T. LeBrun, S. H. Southworth, and L. Young, Nondipolar asymmetries of photoelectron angular distributions, Phys. Rev. Lett. **75**, 4736 (1995).

[5] J. W. Cooper, Photoelectron-angular-distribution parameters for rare-gas subshells, Phys. Rev. A **47**, 1841 (1993).

[6] B. Krässig, E. P. Kanter, S. H. Southworth, R. Guillemin, O. Hemmers, D. W. Lindle, R. Wehlitz, and N. L. S. Martin, Photoexcitation of a dipole-forbidden resonance in helium, Phys. Rev. Lett. **88**, 203002 (2002).

[7] M. Ilchen, G. Hartmann, E. V. Gryzlova, A. Achner, E. Allaria, A. Beckmann, M. Braune, J. Buck, C. Callegari, R. N. Coffee, R. Cucini, M. Danailov, A. De Fanis, A. Demidovich, E. Ferrari, P. Finetti, L. Glaser, A. Knie, A. O. Lindahl, O. Plekan *et al.*, Symmetry breakdown of electron emission in extreme ultraviolet photoionization of argon, Nat. Commun. **9**, 4659 (2018).

[8] F. Lépine, S. Zamith, A. de Snaijer, Ch. Bordas, and M. J. J. Vrakking, Observation of large quadrupolar effects in a slow photoelectron imaging experiment, Phys. Rev. Lett. **93**, 233003 (2004).

[9] C. T. L. Smeenk, L. Arissian, B. Zhou, A. Mysyrowicz, D. M. Villeneuve, A. Staudte, and P. B. Corkum, Partitioning of the linear photon momentum in multiphoton ionization, Phys. Rev. Lett. **106**, 193002 (2011).

[10] B. Willenberg, J. Maurer, B. W. Mayer, and U. Keller, Subcycle time resolution of multi-photon momentum transfer in strong-field ionization, Nat. Commun. **10**, 5548 (2019).

[11] M. Klaiber, E. Yakaboylu, H. Bauke, K. Z. Hatsagortsyan, and C. H. Keitel, Under-the-barrier dynamics in laser-induced relativistic tunneling, Phys. Rev. Lett. **110**, 153004 (2013).

[12] S. Chelkowski, A. D. Bandrauk, and P. B. Corkum, Photon momentum sharing between an electron and an ion in photoionization: From one-photon (photoelectric effect) to multiphoton absorption, Phys. Rev. Lett. **113**, 263005 (2014).

[13] P. L. He, D. Lao, and F. He, Strong field theories beyond dipole approximations in nonrelativistic regimes, Phys. Rev. Lett. **118**, 163203 (2017).

[14] H. C. Ni, S. Brennecke, X. Gao, P. L. He, S. Donsa, I. Březinová, F. He, J. Wu, M. Lein, X. M. Tong, and J. Burgdörfer, Theory of subcycle linear momentum transfer in strong-field tunneling ionization, Phys. Rev. Lett. **125**, 073202 (2020).

[15] A. Hartung, S. Eckart, S. Brennecke, J. Rist, D. Trabert, K. Fehre, M. Richter, H. Sann, S. Zeller, K. Henrichs, G. Kastirke, J. Hoehl, A. Kalinin, M. S. Schöffler, T. Jahnke, L. Ph. H. Schmidt, M. Lein, M. Kunitski, and R. Dörner, Magnetic fields alter strong-field ionization, Nat. Phys. **15**, 1222 (2019).

[16] M. Klaiber, K. Z. Hatsagortsyan, and C. H. Keitel, Subcycle time-resolved nondipole dynamics in tunneling ionization, Phys. Rev. A **105**, 053107 (2022).

[17] A. Ludwig, J. Maurer, B. W. Mayer, C. R. Phillips, L. Gallmann, and U. Keller, Breakdown of the dipole approximation in strong-field ionization, Phys. Rev. Lett. **113**, 243001 (2014).

[18] J. Liu, Q. Z. Xia, J. F. Tao, and L. B. Fu, Coulomb effects in photon-momentum partitioning during atomic ionization by intense linearly polarized light, Phys. Rev. A **87**, 041403(R) (2013).

[19] K. Lin, S. Brennecke, H. Ni, X. Chen, A. Hartung, D. Trabert, K. Fehre, J. Rist, X. M. Tong, J. Burgdörfer, L. Ph. H. Schmidt, M. S. Schöffler, T. Jahnke, M. Kunitski, F. He, M. Lein, S. Eckart, and R. Dörner, Magnetic-field effect in high-order above-threshold ionization, Phys. Rev. Lett. **128**, 023201 (2022).

[20] K. Lin, X. Chen, S. Eckart, H. Jiang, A. Hartung, D. Trabert, K. Fehre, J. Rist, L. Ph. H. Schmidt, M. S. Schöffler, T. Jahnke, M. Kunitski, F. He, and R. Dörner, Magnetic-field effect as a tool to investigate electron correlation in strong-field ionization, Phys. Rev. Lett. **128**, 113201 (2022).

[21] S. Chelkowski, A. D. Bandrauk, and P. B. Corkum, Photon-momentum transfer in multiphoton ionization and in time-resolved holography with photoelectrons, Phys. Rev. A **92**, 051401(R) (2015).

[22] J. Maurer, B. Willenberg, J. Daněk, B. W. Mayer, C. R. Phillips, L. Gallmann, M. Klaiber, K. Z. Hatsagortsyan, C. H. Keitel, and U. Keller, Probing the ionization wave packet and recollision dynamics with an elliptically polarized strong laser field in the nondipole regime, Phys. Rev. A **97**, 013404 (2018).

[23] J. Daněk, M. Klaiber, K. Z. Hatsagortsyan, C. H. Keitel, B. Willenberg, J. Maurer, B. W. Mayer, C. R. Phillips, L. Gallmann, and U. Keller, Interplay between Coulomb-focusing and non-dipole effects in strong-field ionization with elliptical polarization, J. Phys. B **51**, 114001 (2018).

[24] S. Brennecke and M. Lein, Strong-field photoelectron holography beyond the electric dipole approximation: A semiclassical analysis, Phys. Rev. A **100**, 023413 (2019).

[25] S. Brennecke and M. Lein, High-order above-threshold ionization beyond the electric dipole approximation: Dependence on the atomic and molecular structure, Phys. Rev. A **98**, 063414 (2018).

[26] L. Geng, H. Liang, K. Krajewska, L.-Y. Peng, and Q. Gong, Laser-induced electron Fresnel diffraction by XUV pulses at extreme intensity, Phys. Rev. A **104**, L021102 (2021).

[27] B. Willenberg, J. Maurer, U. Keller, J. Daněk, M. Klaiber, N. Teeny, K. Z. Hatsagortsyan, and C. H. Keitel, Holographic interferences in strong-field ionization beyond the dipole approximation: The influence of the peak and focal-volume-averaged laser intensities, Phys. Rev. A **100**, 033417 (2019).

[28] N. Haram, R. T. Sang, and I. V. Litvinyuk, Transverse electron momentum distributions in strong-field ionization: Nondipole and Coulomb focusing effects, J. Phys. B **53**, 154005 (2020).

[29] J. Maurer and U. Keller, Ionization in intense laser fields beyond the electric dipole approximation: Concepts, methods, achievements and future directions, J. Phys. B **54**, 094001 (2021).

[30] S. Brennecke and M. Lein, Nondipole modification of the ac Stark effect in above-threshold ionization, Phys. Rev. A **104**, L021104 (2021).

[31] M. M. Lund and L. B. Madsen, Nondipole photoelectron momentum shifts in strong-field ionization with mid-infrared laser pulses of long duration, J. Phys. B: At. Mol. Opt. Phys. **54**, 165602 (2021).

[32] K. Lin, S. Eckart, A. Hartung, D. Trabert, K. Fehre, J. Rist, L. P. H. Schmidt, M. S. Schöffler, T. Jahnke, M. Kunitski, and R. Dörner, Photoelectron energy peaks shift against the radiation pressure in strong-field ionization, Sci. Adv. **8**, eabn7386 (2022).

[33] M. X. Wang, H. Liang, X. R. Xiao, S. G. Chen, W. C. Jiang, and L. Y. Peng, Nondipole effects in atomic dynamic interference, Phys. Rev. A **98**, 023412 (2018).

[34] L. B. Madsen, Disappearance and reappearance of above-threshold-ionization peaks, Phys. Rev. A **106**, 043118 (2022).

[35] M. Førre and A. S. Simonsen, Nondipole ionization dynamics in atoms induced by intense XUV laser fields, Phys. Rev. A **90**, 053411 (2014).

[36] A. S. Simonsen, T. Kjellsson, M. Førre, E. Lindroth, and S. Selstø, Ionization dynamics beyond the dipole approximation induced by the pulse envelope, Phys. Rev. A **93**, 053411 (2016).

[37] H. R. Reiss, Relativistic strong-field photoionization, J. Opt. Soc. Am. B **7**, 574 (1990).

[38] B. Böning, W. Paufler, and S. Fritzsche, Nondipole strong-field approximation for spatially structured laser fields, Phys. Rev. A **99**, 053404 (2019).

[39] T. Remetter, P. Johnsson, J. Mauritsson, K. Varjú, Y. Ni, F. Lépine, E. Gustafsson, M. Kling, J. Khan, R. López-Martens, K. J. Schafer, M. J. J. Vrakking, and A. L'Huillier, Attosecond electron wave packet interferometry, Nat. Phys. **2**, 323 (2006).

[40] J. Mauritsson, P. Johnsson, E. Mansten, M. Swoboda, T. Ruchon, A. L'Huillier, and K. J. Schafer, Coherent electron scattering captured by an attosecond quantum stroboscope, Phys. Rev. Lett. **100**, 073003 (2008).

[41] E. Goulielmakis, M. Uiberacker, R. Kienberger, A. Baltuska, V. Yakovlev, A. Scrinzi, Th. Westerwalbesloh, U. Kleineberg, U. Heinzmann, M. Drescher, and F. Krausz, Direct measurement of light waves, Science **305**, 1267 (2004).

[42] M. Schultze, M. Fiess, N. Karpowicz, J. Gagnon, M. Korbman, M. Hofstetter, S. Neppl, A. L. Cavalieri, Y. Komninos, Th. Mercouris, C. A. Nicolaides, R. Pazourek, S. Nagele, J. Feist, J. Burgdorfer, A. M. Azzeer, R. Ernstorfer, R. Kienberger, U. Kleineberg, E. Goulielmakis *et al.*, Delay in photoemission, Science **328**, 1658 (2010).

[43] J. Tan, S. Xu, X. Han, Y. Zhou, M. Li, W. Cao, Q. Zhang, and P. Lu, Resolving and weighing the quantum orbits in strong-field tunneling ionization, Adv. Photon. **3**, 035001 (2021).

[44] M. H. Mustary, L. Xu, W. Wu, N. Haram, D. E. Laban, H. Xu, F. He, R. T. Sang, and I. V. Litvinyuk, Attosecond delays of high-harmonic emissions from hydrogen isotopes measured by XUV interferometer, Ultrafast Sci. **2022**, 9834102 (2022).

[45] S. Pan, C. Hu, Z. Zhang, P. Lu, C. Lu, L. Zhou, J. Wang, F. Sun, J. Qiang, H. Li, H. Ni, X. Gong, F. He, and J. Wu, Low-energy protons in strong-field dissociation of H_2^+ via dipole-transitions at large bond lengths, Ultrafast Sci. **2022**, 9863548 (2022).

[46] M. Yu, K. Liu, M. Li, J. Yan, C. Cao, J. Tan, J. Liang, K. Guo, W. Cao, P. Lan, Q. Zhang, Y. Zhou, and P. Lu, Full experimental determination of tunneling time with attosecond-scale streaking method, Light Sci. Appl. **11**, 215 (2022).

[47] S. Brennecke and M. Lein, High-order above-threshold ionization beyond the electric dipole approximation, J. Phys. B **51**, 094005 (2018).

[48] M. Førre and A. S. Simonsen, Generalized velocity-gauge form of the light-matter interaction Hamiltonian beyond the dipole approximation, Phys. Rev. A **93**, 013423 (2016).

[49] M. Førre and S. Selstø, Schrödinger formulation of the nondipole light-matter interaction consistent with relativity, Phys. Rev. A **101**, 063416 (2020).

[50] J. Liang, Y. Zhou, W. C. Jiang, M. Yu, M. Li, and P. Lu, Zeeman effect in strong-field ionization, Phys. Rev. A **105**, 043112 (2022).

[51] J. Liang, W. C. Jiang, Y. Liao, Q. Ke, M. Yu, M. Li, Y. Zhou, and P. Lu, Intensity-dependent angular distribution of low-energy electrons generated by intense high-frequency laser pulse, Opt. Express **29**, 16639 (2021).

[52] J. Liang, W. C. Jiang, S. Wang, M. Li, Y. Zhou, and P. Lu, Atomic dynamic interference in intense linearly and circularly polarized XUV pulses, J. Phys. B **53**, 095601 (2020).

[53] J. Liang, Y. Zhou, Y. Liao, W. Jiang, M. Li, and P. Lu, Direct visualization of deforming atomic wavefunction in ultraintense high-frequency laser pulses, Ultrafast Sci. **2022**, 9842716 (2022).

[54] D. G. Arbó, J. E. Miraglia, M. S. Gravielle, K. Schiessl, E. Persson, and J. Burgdörfer, Coulomb-Volkov approximation for near-threshold ionization by short laser pulses, Phys. Rev. A **77**, 013401 (2008).

[55] N. J. Kylstra, R. M. Potvliege, and C. J. Joachain, Photon emission by ions interacting with short intense laser pulses: Beyond the dipole approximation, J. Phys. B: At. Mol. Opt. Phys. **34**, L55 (2001).

[56] W.-C. Jiang and X.-Q. Tian, Efficient Split-Lanczos propagator for strong-field ionization of atoms, Opt. Express **25**, 26832 (2017).

[57] N. J. Kylstra, R. A. Worthington, A. Patel, P. L. Knight, J. R. Vázquez de Aldana, and L. Roso, Breakdown of stabilization of atoms interacting with intense, high-frequency laser pulses, Phys. Rev. Lett. **85**, 1835 (2000).

[58] J. Grochmalicki, M. Lewenstein, and K. Rzążewski, Stabilization of atoms in superintense laser fields: Is it real? Phys. Rev. Lett. **66**, 1038 (1991).

[59] J. R. Vázquez de Aldana, N. J. Kylstra, L. Roso, P. L. Knight, A. Patel, and R. A. Worthington, Atoms interacting with intense, high-frequency laser pulses: Effect of the magnetic-field component on atomic stabilization, Phys. Rev. A **64**, 013411 (2001).

[60] M. Førre, S. Selstø, J. P. Hansen, and L. B. Madsen, Exact nondipole Kramers-Henneberger form of the light-atom Hamiltonian: An application to atomic stabilization and photoelectron energy spectra, Phys. Rev. Lett. **95**, 043601 (2005).

[61] M. Førre, J. P. Hansen, L. Kocbach, S. Selstø, and L. B. Madsen, Nondipole ionization dynamics of atoms in superintense high-frequency attosecond pulses, Phys. Rev. Lett. **97**, 043601 (2006).

[62] W.-C. Jiang and J. Burgdörfer, Dynamic interference as signature of atomic stabilization, Opt. Express **26**, 19921 (2018).

[63] W.-C. Jiang, M.-X. Wang, L.-Y. Peng, and J. Burgdörfer, Signatures of stabilization in the angle-resolved photoemission by an ultrashort intense XUV laser pulse, Phys. Rev. A **105**, 023104 (2022).

[64] K. Toyota, O. I. Tolstikhin, T. Morishita, and S. Watanabe, Interference substructure of above-threshold ionization peaks in the stabilization regime, Phys. Rev. A **78**, 033432 (2008).

[65] P. V. Demekhin and L. S. Cederbaum, Dynamic interference of photoelectrons produced by high-frequency laser pulses, Phys. Rev. Lett. **108**, 253001 (2012).

[66] F. Quéré, J. Itatani, G. L. Yudin, and P. B. Corkum, Attosecond spectral shearing interferometry, Phys. Rev. Lett. **90**, 073902 (2003).

[67] U. Saalmann and J. M. Rost, Proper time delays measured by optical streaking, Phys. Rev. Lett. **125**, 113202 (2020).